Magnetic ground state in $FeTe_2$, VS_2, and $NiTe_2$ monolayers: Antiparallel magnetic moments at chalcogen atoms

Mehmet Aras and Çetin Kılıç*
Department of Physics, Gebze Technical University, 41400 Kocaeli, Turkey

S. Ciraci†
Department of Physics, Bilkent University, 06800 Ankara, Turkey

(Received 27 August 2019; revised manuscript received 4 February 2020; accepted 5 February 2020; published 21 February 2020)

Our analysis based on the results of hybrid and semilocal density-functional calculations with and without Hubbard U correction for on-site Coulomb interactions reveals the true magnetic ground states of three transition-metal dichalcogenide monolayers, viz., $FeTe_2$, VS_2, and $NiTe_2$, which comprise inhomogeneous magnetic moment configurations. In contrast to earlier studies considering only the magnetic moments of transition-metal atoms, the chalcogen atoms by themselves have significant, antiparallel magnetic moments owing to the spin polarization through p-d hybridization. The latter is found to be true for both H and T phases of $FeTe_2$, VS_2, and $NiTe_2$ monolayers. Our predictions show that the $FeTe_2$ monolayer in its lowest-energy structure is a half metal, which prevails under both compressive and tensile strains. Half metallicity occurs also in the $FeTe_2$ bilayer but disappears in thicker multilayers. The VS_2 monolayer is a magnetic semiconductor; it has two different band gaps of different character and widths for different spin polarization. The $NiTe_2$ monolayer, which used to be known as a nonmagnetic metal, is indeed a magnetic metal with a small magnetic moment. These monolayers with intriguing electronic and magnetic properties can attain new functionalities for spintronic applications.

DOI: 10.1103/PhysRevB.101.054429

I. INTRODUCTION

Mono- and multilayers of transition-metal dichalcogenides (MX_2) [1–5] showing high stability and critical physical and chemical properties [6–11] are now widely accepted to be a class of two-dimensional (2D) materials which are in various aspects superior to 2D group-IV elements and group-III-V compounds and offer a variety of potential applications. While the majority of them are metallic, MX_2 with $M =$ Cr, Mo, and W are generally semiconductors showing metal-insulator transition with electrostatic charging [12–14] or direct-indirect band-gap transition with the number of layers [6]. As the realization of 2D magnetic crystals was a great challenge [15], spin-polarized calculations [5] revealed that the magnetic ground state can be indigenous to some MX_2 monolayers, since one of their constituents can be a transition-metal atom (e.g., $M =$ Sc, Ti, V, Cr, Mn, Fe, Ni). It has been contemplated that the magnetic long-range order of specific layered three-dimensional (3D) MX_2 crystals would persist even after the exfoliation of MX_2 monolayers. With an intrinsic magnetic moment, the MX_2 monolayer can be a ferromagnetic metal, ferromagnetic semiconductor, even a half metal [16]. The superexchange interaction [17,18] between nearest M atoms through the adjacent X atom has been considered as a mechanism leading to ferromagnetic ground state. In some monolayers, spin-orbit interactions resulting in spin-valley coupling can lead to critical spintronic properties [19,20].

Much earlier, theoretical models, such as 2D Ising, XY, and Heisenberg models, indicated that the magnetic order in 2D monolayers is rather complex and depends on a spin dimensionality of 1 to 3, even if the long-range order of magnetic moments in 3D crystals can occur for $T > 0$ K, and that of 1D systems at $T = 0$ K. In particular, the magnetic order may deviate strongly by going from three to two dimensions. However, recent observations of magnetic order in 2D monolayers like $CrGeTe_3$ [21] and CrI_3 [22] have reactivated interest in magnetic MX_2 monolayers by bringing the second- and third-nearest-neighbor exchange interactions [23] and magnetic anisotropy [24] into focus. Furthermore, owing to the weak van der Waals interlayer interaction, multilayers of MX_2 and their heterostructures [25–30] have been considered as novel materials [6,31,32] with intriguing electronic and magnetic properties. It is anticipated that confinements of electrons into 2D monolayers or very thin films can lead to interesting dimensionality effects in magnetic states.

Owing to the most recent studies unveiling various magnetic features, the range of interest in these magnetic 2D MX_2-based materials has expanded tremendously [16]. On the theoretical side, the ground-state magnetic order of some transition-metal dichalcogenide (TMD) monolayers and modifying their magnetic properties by external agents have been

*cetin_kilic@gtu.edu.tr
†ciraci@fen.bilkent.edu.tr

studied intensely with the aid of density-functional theory (DFT) calculations performed at various levels of approximations. Now the prime issue is whether these studies can conclude with similar predictions on the magnetic properties despite the different approximations used for the electron-electron interaction. In fact, earlier DFT calculations using semilocal functionals yielded unrealistic magnetic ground states for magnetic TMD monolayers. This issue is crucial for an understanding of magnetic 2D MX_2 crystals, but remains unresolved so far.

This study investigates the magnetic properties of three selected TMD monolayers, viz., $FeTe_2$, VS_2, and $NiTe_2$, one of which (VS_2) has been widely studied. Because of their potential applications, binary nickel tellurides including their mono- and multilayers have been an active subject of experimental and theoretical studies [33,34]. Recent studies have conveyed that $FeTe_2$ holds great promise in spintronics [29,35]. Our objective is to present an extensive analysis in order to examine how the magnetic ground states and resulting electronic properties of three selected TMD monolayers depend on the method of calculation and the level of approximation. To this end, we performed not only semilocal DFT calculations within the local density approximation (LDA) and generalized gradient approximation (GGA) using the Perdew-Burke-Ernzerhof (PBE) functional [36] with and without Hubbard U correction for on-site Coulomb interactions [37], but also hybrid DFT calculations using the Heyd-Scuseria-Ernzerhof (HSE) functional [38,39] with and without spin-orbit coupling (SOC). We draw our conclusions based on the qualitative agreement between the results of DFT + U and HSE calculations, since the strong correlations that are important for describing d electrons of transition metals are only partly taken into account in either of the DFT + U and HSE calculations, which are ignored in semilocal DFT calculations [40].

We find that while the VS_2 monolayer is a magnetic semiconductor with a net magnetic moment $\mu = 1\mu_B$ per formula unit, the $FeTe_2$ monolayer is a half metal with integer magnetic moment of $\mu = 2\mu_B$. While the DFT + U calculations predict *no* spin polarization for the $NiTe_2$ monolayer in agreement with the semilocal DFT calculations [29], the HSE results indicate that the $NiTe_2$ monolayer is a magnetic metal with a relatively small magnetic moment $\mu < 1\mu_B$. This disagreement is addressed by comparison with very recent experimental findings [41,42]. It is noteworthy that owing to the spin polarization of chalcogen atoms through p-d hybridization the studied TMD monolayers have magnetic ground states with local magnetic moments at chalcogen atoms antiparallel to those at transition-metal atoms. This situation is reminiscent of ferrimagnetic order.

The spin polarization of oxygen atoms via p-d hybridization was recently reported for 3D transition-metal oxides [43,44] and iron oxide clusters [45], and causes substantial changes in the exchange interactions. In addition, the chalcogen atoms in 1T-CrX_2 (X = Se, Te) monolayers are also found to be spin polarized [46]. In line with these findings, our results show that the p-d hybridization renders the chalcogen p band spin-polarized in $FeTe_2$, VS_2, and $NiTe_2$ monolayers. Antiparallel local magnetic moments in different atoms of diverse 3D Heusler compounds (e.g., MnCrSb, Mn_3Ga, and NiMnSb) with compensating magnetic moments fulfilling the Slater-Pauling rule [47–49], zincblende Mn-doped transition-metal dichalcogenides [50], and half-metallic Mn_2VAl [51] and $LuCu_3Mn_4O_{12}$ [52] showing ferrimagnetic order were reported earlier. Furthermore, the 2D MXene $Mo_3N_2F_2$ was recently predicted to be a ferrimagnetic half metal [53]. This study, however, expounds on the magnetic ground states with antiparallel alignment of local magnetic moments at transition-metal and chalcogen atoms in three representative 2D single-layer transition-metal dichalcogenides with half-metallic, semiconducting, and metallic behaviors.

It is sensible to distinguish if a material has a parallel, antiparallel, or inhomogeneous spin arrangement, especially from an application point of view. For example, an advantage of using an antiferromagnet or ferrimagnet in lieu of a ferromagnet is to reduce the stray fields in spintronic devices such as magnetic tunnel junctions (MTJs) [54–57]. The use of magnets with negative exchange coupling brings also advantages in spin transfer applications, owing to a much shorter time scale of magnetization dynamics and reversal compared to that of a ferromagnet with positive exchange coupling [58–61]. In view of the present results, MX_2 monolayers with inhomogeneous magnetic moment distribution can find use in 2D MTJs [62] and spin transfer applications. This may extend the domain of interest in magnetic 2D MX_2-based materials to spintronic devices.

In the rest of the paper, we present and discuss our calculation results in Sec. III, following a brief description of computational settings in Sec. II, and conclude with a short summary in Sec. IV.

II. METHOD

To investigate the magnetic and electronic states of $FeTe_2$, VS_2, and $NiTe_2$, we performed hybrid as well as semilocal DFT calculations by using the Vienna Ab initio Simulation Package [63] (VASP) together with its projector-augmented wave (PAW) potential database [64]. Spin polarization was taken into account in these calculations, some of which were repeated with spin-orbit coupling for the sake of comparison. The hybrid DFT calculations were carried out with the HSE06 functional [38,39]. The semilocal calculations were performed using either the Ceperley-Alder functional [65] or the PBE functional [36], with and without Hubbard U correction for on-site Coulomb interactions [37]. The states in the electron configurations $3d^74s^1$, $3d^94s^1$, $3p^63d^44s^1$, $5s^25p^4$, and $3s^23p^4$ for iron, nickel, vanadium, tellurium, and sulfur, respectively, were treated as valence states. The electronic wave functions were expanded into a plane-wave basis set with a cutoff energy of 400 eV. Increasing the latter to 600 eV for the $FeTe_2$ monolayer resulted in a variation of 0.25 meV in the total energy per formula unit and yielded no variation in the magnetic moment, both of which imply a high level of convergence with respect to the cutoff energy.

We used 1×1 supercells based on the 2D monolayer unit cells (with one MX_2 unit), including a vacuum spacing of 20 Å between periodic images of the monolayer along the direction perpendicular to the monolayer. We performed structural optimizations where the equilibrium value of the 2D lattice constants was determined via minimization of the total energy

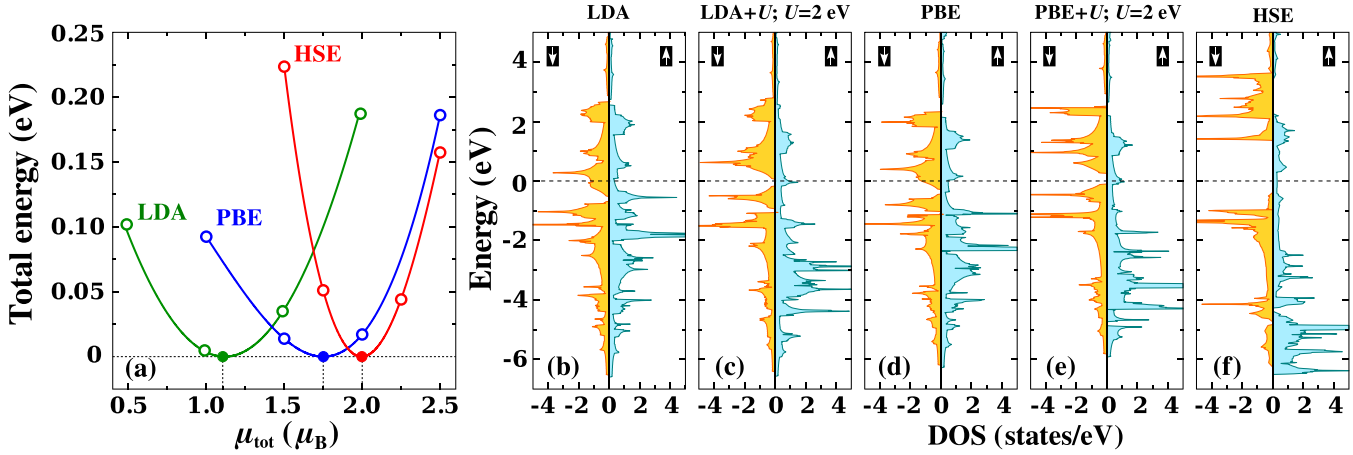

FIG. 1. Magnetic ground state of $FeTe_2$ monolayer in H structure predicted by hybrid, semilocal DFT, and DFT + U calculations. (a) The total energies as a function of the magnetic moment per formula unit μ_{tot}, obtained from the LDA ($U = 0$), PBE ($U = 0$), and HSE calculations. (b)–(f) The densities of states (DOS) of the minority (spin-down, ↓) and majority (spin-up, ↑) states of $FeTe_2$ within various approximations for the electron-electron interaction.

and the ionic positions were relaxed until the residual forces on atoms were reduced to be smaller than 10^{-2} eV/Å. The Brillouin zone sampling was done using $12 \times 12 \times 1$ ($FeTe_2$ and $NiTe_2$) or $18 \times 18 \times 1$ (VS_2) **k**-point meshes generated according to the Monkhorst-Pack scheme [66]. Using the optimized structures, we performed electronic structure calculations in order to obtain the magnetic and electronic states of $FeTe_2$, VS_2, and $NiTe_2$. The density derived electrostatic and chemical (DDEC) spin partitioning technique [67,68] was employed to divide the magnetic moment μ_{tot} per formula unit among the constituent atoms M and X, which was preferred to ensure $\mu_{tot} = \mu_M + 2\mu_X$.

In order to assess the stability of the magnetic ground state of $FeTe_2$, we scanned a variety of competing magnetic configurations generated by using 2×2 supercells (SCs) that contain four $FeTe_2$ units, and computed the total energy E_{SC} using HSE for a range of *fixed* values of the supercell magnetic moment M_{SC}. We also studied the variation of E_{SC} with the total magnetic moments of the Fe and Te sublattices in order to identify the character of exchange interactions between the Fe-Fe, Fe-Te, and Te-Te atom pairs.

III. RESULTS AND DISCUSSION

Earlier studies based on dynamical and thermal stability analysis have ensured the stability of the $FeTe_2$ (e.g., Refs. [5,35]), VS_2 (e.g., Refs. [5,69,70]), and $NiTe_2$ (e.g., Refs. [5,29]) monolayers in *both* H and T structures with trigonal-prismatic and octahedral coordinations, respectively. For the difference between the optimized total energies of H and T phases, $E_H - E_T$, we obtained the following values (in meV per formula unit): $E_H - E_T = -44$ (LDA), -14 (PBE), and -65 (HSE) for the $FeTe_2$ monolayer; -18 (LDA), -41 (PBE), and -59 (HSE) for the VS_2 monolayer; and 281 (LDA), 224 (PBE), and 334 (HSE) for the $NiTe_2$ monolayer. Hence, regardless of the method of calculation, the H (T) phase has lower energy for $FeTe_2$ and VS_2 ($NiTe_2$) monolayers. Therefore, in this section we present the results for H-$FeTe_2$, H-VS_2, and T-$NiTe_2$ mono- and multilayers, and also mention some results for the higher-energy structures for comparison.

The LDA and PBE calculations with $U = 0$ fail to yield the true magnetic ground state and electronic structure for the $FeTe_2$ monolayer, both of which result in a ferromagnetic metallic state with noninteger values of the magnetic moment. After adding a Hubbard U term to either LDA or PBE functionals, a band gap starts to open in the density of states (DOS) of minority spins for $U > 1.5$ eV. Notably, both PBE + U and LDA + U with $U = 2$ eV predict a small band gap of the minority spin states but a metallic state for majority spins. The net (total) magnetic moment is calculated to be $\mu_{tot} = 2\mu_B$ using both methods. As U increases, the band gap of minority spin states increases, but μ_{tot} remains fixed at $2\mu_B$. The HSE calculations also predict $\mu_{tot} = 2\mu_B$, and a band gap of 1.77 eV, which is wider than that of LDA even with $U =$ 5 eV. Nevertheless, except for the value of the minority band gap, the PBE + U and HSE calculations yield quite similar electronic structures as seen in Fig. 1, and also produce the same integer value for the magnetic moment. This agreement between the DFT + U and HSE results (qualitative for the spin-polarized electronic structure and minority band gap) demonstrates that semilocal DFT calculations, where strong correlations needed for the proper description of d electrons of transition metals are missing, would not necessarily yield the correct magnetic ground state of MX_2 monolayers. The integer values of μ_{tot} (associated with either the magnetic semiconductor or half-metallic behavior) are important and pave the way for a variety of spintronic applications. Apparently, such an important property of bare MX_2 monolayers could have been skipped if the electron-electron interaction were not treated properly.

The magnetic ground state of three transition-metal dichalcogenide monolayers, viz., $FeTe_2$, VS_2, and $NiTe_2$, calculated with HSE are characterized by plotting the isosurfaces of the spin density $\rho_S(\mathbf{r}) = \rho_\uparrow(\mathbf{r}) - \rho_\downarrow(\mathbf{r})$ in Fig. 2(a), where $\rho_\uparrow(\mathbf{r})$ and $\rho_\downarrow(\mathbf{r})$ denote the charge density of spin-up and spin-down states, respectively. It is seen that the charge densities localized around the transition-metal and chalcogen atoms

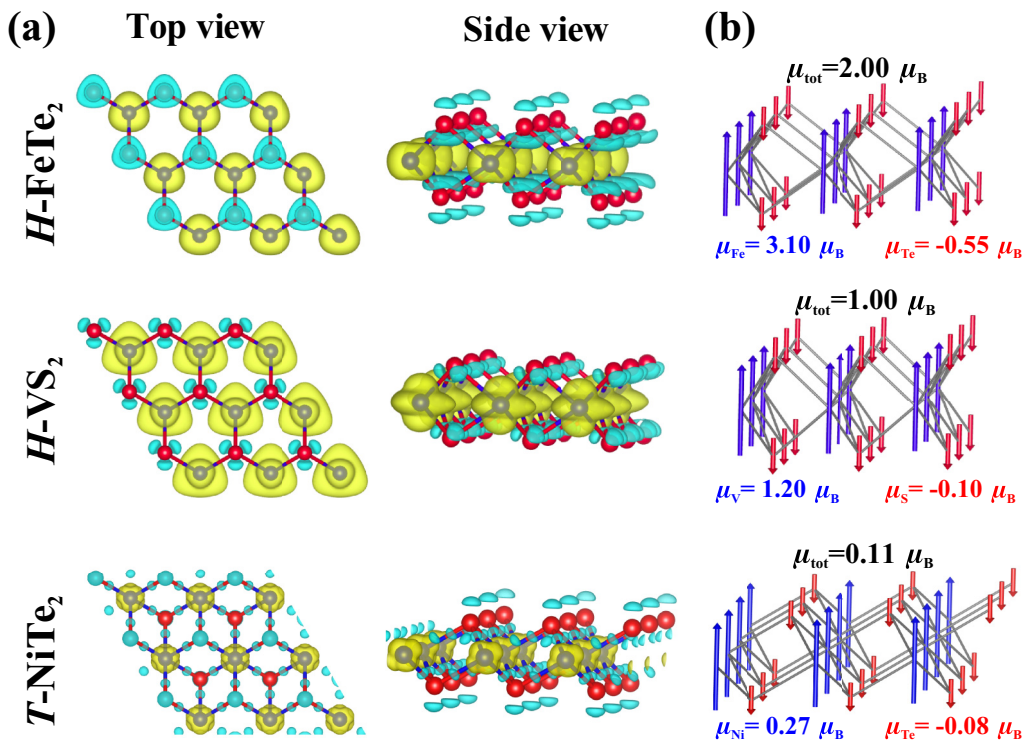

FIG. 2. (a) Top and side views of the isosurfaces of the HSE-calculated spin density $\rho_S(\mathbf{r})$ for $FeTe_2$, VS_2, and $NiTe_2$ monolayers in their lowest-energy structures, corresponding to the isovalues of $+0.01$, $+0.0075$, and $+0.005$ (yellow) and -0.01, -0.0075, and -0.005 (cyan) $\mu_B/\text{Å}^3$, respectively. (b) Local magnetic moments μ_M and μ_X calculated at the transition-metal (M) and chalcogen (X) atoms, respectively. The blue and red arrows (located at the M and X atom sites, respectively) are drawn, not to scale, to indicate opposing spin polarization of the transition-metal and chalcogen atoms.

originate from states of different spin polarizations. Thus, contrary to earlier assumptions which assign the net magnetic moment only to the transition-metal atoms, the chalcogen atoms by themselves have a significant magnetic moment in opposite polarization. The latter is further elaborated by dividing the total magnetic moment μ_{tot} among the constituent atoms to yield $\mu_{tot} = \mu_M + 2\mu_X$, which is done by the DDEC spin partitioning technique [67,68]. The alignment of local magnetic moments (μ_M and μ_X) is shown in Fig. 2(b), which is reminiscent of ferrimagnetic order. Hence, the magnetic ground state in MX_2 monolayers here, some of which were identified earlier as ferromagnetic [71–75], comprise inhomogeneous magnetic moment configurations owing to significant magnetic moments at chalcogen atoms antiparallel to those at transition-metal atoms. We believe that this is an important, insofar fundamental, conclusion, conveying the correct magnetic ground state of $FeTe_2$, VS_2, and $NiTe_2$ monolayers. This conclusion arrived at in the absence of the spin-orbit coupling shows, contrary to prevailing assumptions [16], that the magnetic order in 2D MX_2-based materials need *not* be attributed to the magnetocrystalline anisotropy.

Figure 3(a) displays the bar plots of μ_{tot} and its transition-metal and chalcogen components, i.e., μ_M and $2\mu_X$, respectively, for comparing the results obtained at five levels of approximations. It is seen that the DFT + U and HSE calculations yield either the same or very close values for μ_{tot} of $FeTe_2$ and VS_2 monolayers, which makes it clear that μ_{tot} is substantially underestimated in the semilocal DFT calculations. Similarly, whereas the semilocal DFT calculations with $U = 0$ yield a negligibly small μ_X (cf. Refs. [71,75]), the DFT + U and HSE results show that μ_X is indeed not negligible compared to μ_{tot}. This is seen better in Fig. 3(b), where the ratios μ_M/μ_{tot} and $2\mu_X/\mu_{tot}$ are plotted with respect to each other, which signify the M and X contributions to the magnetic moment, respectively. On the other hand, it can be likely that μ_M and μ_X are both overestimated in the DFT + U and HSE calculations even though they yield a more reliable value for μ_{tot}, which is supported by the linear correlation between $2\mu_X/\mu_{tot}$ and μ_M/μ_{tot} in Fig. 3(b). Furthermore, it is known that the magnetic moment of transition-metal atoms in their elemental *metallic* solids can be substantially overestimated by HSE, corresponding to an error as high as 35% for elemental Ni solid [76]. Contrary to the latter, the HSE calculations for *half metals* such as GdN can yield magnetic moments in close agreement with experiment [77]. Fortunately, the metallic $NiTe_2$ monolayer provides a useful example for the assessment of the HSE-calculated magnetic moments. The HSE calculations yield small but *nonzero* values for both μ_{Ni} and μ_{Te}, indicating an antiparallel alignment of the Ni and Te moments, whereas $\mu_{Ni} = \mu_{Te} = 0$ in all other (LDA, PBE, LDA + U, and PBE + U) calculations [cf. Fig. 3(a)]. Experimental studies on single-crystalline $NiTe_x$ bulk samples [41] as well as $NiTe_x$ nanorods [42], both with chemical bonding reminiscent of that in the T-$NiTe_2$ monolayer, show that the magnetic moment of $NiTe_x$ decreases with increasing x. Even if this behavior is attributable to the presence of diamagnetism in $NiTe_x$ nanorods [42], an antiparallel alignment of the Ni and Te moments is inferred from it because the diamagnetism

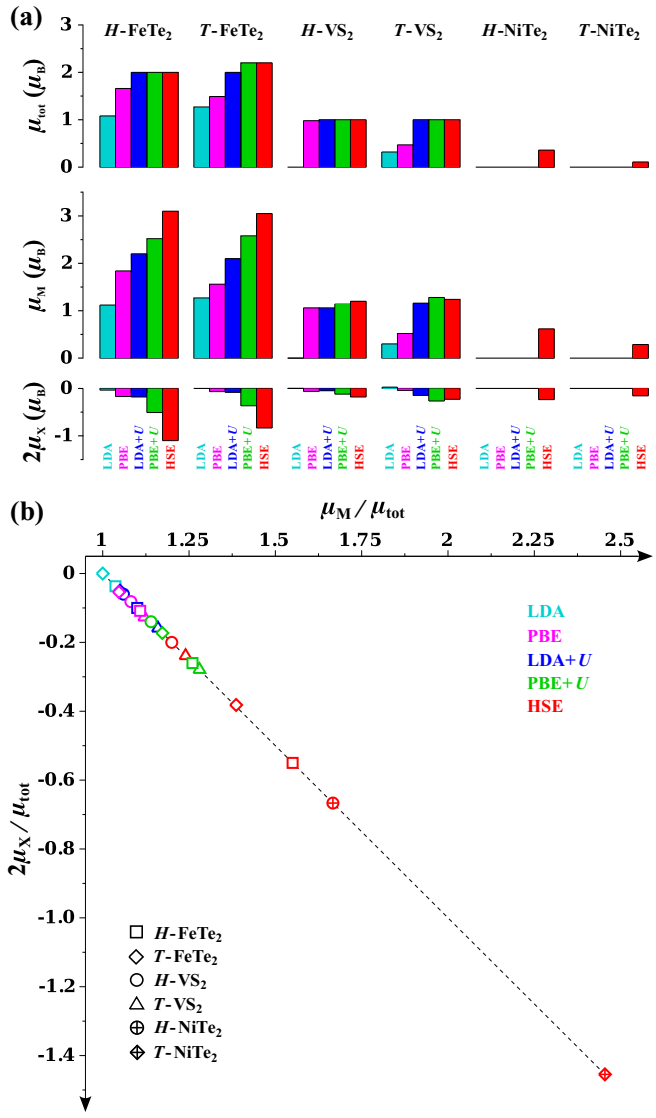

FIG. 3. (a) The bar plots of μ_{tot} and its components μ_M and $2\mu_X$, obtained at five levels of approximation, i.e., LDA, PBE, LDA + U, PBE + U, and HSE. (b) The plot of $2\mu_X/\mu_{tot}$ with respect to μ_M/μ_{tot}.

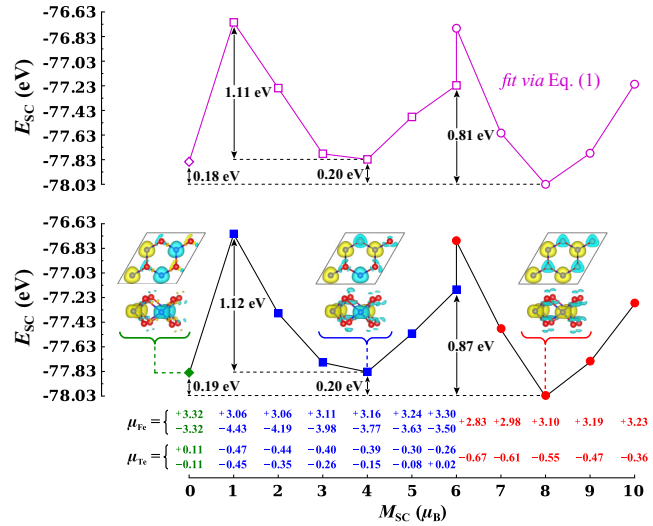

FIG. 4. The variation of the supercell total energy E_{SC} with the supercell magnetic moment M_{SC}. The solid and open symbols represent the HSE-calculated and fitted points, respectively. The solid lines connecting the calculated as well as fitted points are drawn to guide the eye. The isosurfaces of the spin density for the $M_{SC} = 0\mu_B$, $4\mu_B$, and $8\mu_B$ configurations are shown as insets.

was *not* detected in bulk $NiTe_2$ single crystals [41]. As long as neither semilocal DFT nor DFT + U calculations yield an antiparallel alignment of μ_{Ni} and μ_{Te} as in experimental and HSE results, we think that the hybrid rather than other DFT calculations produce reliable estimates for the atomic moments in the $NiTe_2$ monolayer.

The stability of the magnetic ground state of $FeTe_2$ depicted in Fig. 2(b) is assessed by comparing the total energies E_{SC} of a variety of competing magnetic configurations generated by using 2×2 supercells, as shown in Fig. 4. It is to be noted that various types of magnetic configurations where the magnetic moments of the second-neighbor Fe atoms are parallel (the red symbols) or antiparallel (the green and blue symbols in Fig. 4) are included, which were obtained via minimization of the total energy. It is seen from the HSE-calculated energy profile plotted in Fig. 4 that $M_{SC} = 0$ and $M_{SC} = 4\mu_B$ configurations have almost the same energy that is 0.19 eV higher than the energy of the configuration corresponding to $M_{SC} = 8\mu_B$. Hence the $M_{SC} = 8\mu_B$ configuration with magnetic order as shown in Fig. 2(b) has the lowest energy, which is then the magnetic ground state in $FeTe_2$. It should also be noticed that the system needs to overcome large energy barriers of 0.87 and 1.12 eV in order to have a transition from this configuration to the $M_{SC} = 4\mu_B$ and $M_{SC} = 0$ configurations, respectively. For VS_2 and $NiTe_2$ monolayers, the HSE calculations using 2×2 supercells predict that the antiferromagnetic state has an energy higher than that of the ground state by 0.58 and 0.15 eV, respectively.

In order to identify the character of exchange interactions between the Fe-Fe, Fe-Te, and Te-Te atom pairs, we study the variation of the total energy also with the total magnetic moments of the Fe and Te sublattices. A parametrization of E_{SC} as a function of $M_{Fe} = \sum_{Fe} \mu_{Fe}/\mu_B$ and $M_{Te} = \sum_{Te} \mu_{Te}/\mu_B$ according to

$$\begin{aligned} E_{SC} &= E_0 + E_2 + E_4, \\ E_2 &= -\tfrac{1}{2}\left(\gamma_{11} M_{Fe}^2 + 2\gamma_{12} M_{Fe} M_{Te} + \gamma_{22} M_{Te}^2\right), \\ E_4 &= g_1 M_{Fe}^4 + g_2 M_{Fe}^3 M_{Te} + g_3 M_{Fe}^2 M_{Te}^2 + g_4 M_{Fe} M_{Te}^3 \\ &\quad + g_5 M_{Te}^4, \end{aligned} \tag{1}$$

is presented in magenta in Fig. 4. The inclusion of the E_2 and E_4 terms in Eq. (1) are in line with the Néel [78,79] and Landau [80,81] theories, respectively. As seen from their values in Fig. 4, the local magnetic moments μ_{Fe} and μ_{Te} exhibit significant variation among the scanned magnetic states, which is indicative for non-Heisenberg exchange interactions [44,82]. Thus we took into account not only the usual bilinear exchange interactions (through E_2) but also biquadratic exchange interactions [83,84] (through E_4), which enabled us to obtain a satisfactory parametrization. A weighted fit yields $\gamma_{11} = -0.108$, $\gamma_{12} = -0.305$, $\gamma_{22} = -0.848$, $g_1 = -0.001$,

TABLE I. The HSE-calculated values of the local magnetic moments μ_M and μ_X in antiferromagnetic ($M_{SC} = 0$) and magnetic ground ($M_{SC} \neq 0$) states.

Monolayer	M_{SC} (μ_B)	μ_M (μ_B)	μ_X (μ_B)
H-$FeTe_2$	8	+3.10	−0.55
	0	±3.32	±0.11
H-VS_2	4	+1.20	−0.10
	0	±0.58	±0.02
T-$NiTe_2$	0.44	+0.27	−0.08
	0	±0.27	±0.02
H-$NiTe_2$	1.44	+0.60	−0.12
	0	±0.49	±0.02

TABLE II. The values of the supercell magnetic moment M_{SC} and the local magnetic moments μ_{Fe} and μ_{Te} for the H-$FeTe_2$ monolayer, obtained from the collinear and noncollinear PBE + U calculations with and without spin-orbit coupling (SOC), respectively. Noncollinear configurations are indicated by "In plane" ("Out of plane") in the second column, which means that the magnetization vectors are aligned in (perpendicular to) the monolayer plane.

Method		M_{SC} (μ_B)	μ_{Fe} (μ_B)	μ_{Te} (μ_B)
PBE + U	Collinear	8	+2.524	−0.262
		0	±3.014	±0.052
PBE + U + SOC	In plane	8.064	+2.526	−0.255
		0	±3.004	±0.053
	Out of plane	8.088	+2.526	−0.252
		0.023	±2.961	±0.056

$g_2 = -0.013$, $g_3 = -0.053$, $g_4 = -0.096$, $g_5 = -0.062$, and $E_0 = -77.847$ eV, where the biquadratic coefficients turn out to be much smaller than the bilinear coefficients. It should be noted that the fit via Eq. (1) is numerically quite satisfactory since it reproduces not only the energy differences among the $M_{SC} = 0\mu_B$, $4\mu_B$, and $8\mu_B$ configurations but also the barrier heights accurately, as indicated in Fig. 4. Since the mean-field (γ) coefficients and the exchange (J) constants are usually of the same sign [80], having $\gamma_{11}, \gamma_{12}, \gamma_{22} < 0$ means that the exchange couplings between the Fe-Fe, Fe-Te, and Te-Te atom pairs are *antiferromagnetic* (i.e., negative). Negative exchange coupling between its constituent atoms may facilitate the use of the $FeTe_2$ monolayer in spin transfer applications. This finding also reminds us of spinel ferrites (decomposed into the sublattices A and B) in which the A-A, A-B, and B-B antiferromagnetic interactions lead to ferrimagnetic order [78,84,85]. It is nevertheless to be noted that antiferromagnetic Fe-Fe and Te-Te interactions in the $FeTe_2$ monolayer obtained from the above fit contrast with the ground state predicted from the HSE calculations.

It has been customary to deduce the exchange coupling constants from the energy differences between antiferromagnetic configurations and the magnetic ground state and to estimate the transition temperature to paramagnetic state via either a mean-field expression for Curie temperature T_C or Monte Carlo simulations, which was also done for the VS_2 monolayer [72,73,86] and nanoribbons [87], and the $FeTe_2$ monolayer [74]. As seen from the predicted values of T_C collected in Table S1 of the Supplemental Material [88], the estimates scatter considerably, which can partly be attributed to different approximations for electron-electron interaction. In contrast with these efforts, our findings indicate that this type of approach is in fact *not* adequate for MX_2 monolayers that have a magnetic ground state with antiparallel alignment of local magnetic moments at M and X atoms, which are *not* describable by classical Heisenberg or Ising models owing to the non-Heisenberg character of the exchange interactions in these systems. The latter is manifested by the substantial variation of the local magnetic moments μ_M and μ_X among the scanned magnetic states in Fig. 4 as mentioned above, which is also clear from the values of μ_M and μ_X in Table I. It should, for example, be noticed that the magnitude of the local moments of vanadium in the VS_2 monolayer in the antiferromagnetic state is $0.58\mu_B$, which is substantially smaller than $\mu_V = 1.2\mu_B$ for the magnetic ground state. A significant reduction of μ_X in the antiferromagnetic state is also noticeable. It is also revealing to note that a satisfactory parametrization of E_{SC} as a function of the sublattice magnetic moments within a mean-field approximation for the Heisenberg Hamiltonian is *not* obtained even if the non-Heisenberg character of the exchange interactions in the MX_2 monolayer is overlooked, as analyzed in Fig. S1 in the Supplemental Material [88].

In order to examine the effect of SOC on the magnetic order in the H-$FeTe_2$ monolayer, we present the values of μ_{Fe} and μ_{Te} in Table II, which are obtained from the collinear and noncollinear PBE + U calculations with and without SOC, respectively, performed by using 2×2 supercells. It is seen that the inclusion of SOC results in a *slight* increase in M_{SC} for both in-plane and out-of-plane configurations. Corresponding to the latter, μ_{Fe} and μ_{Te} also vary slightly. More importantly, the Fe and Te moments are found to align antiparallel in noncollinear calculations, except for the out-of-plane configuration with $M_{SC} = 0.023\mu_B$ (where the μ_{Fe} and μ_{Te} vectors deviate slightly from the antiparallel alignment by less than 4°). Among the noncollinear configurations, the in-plane configuration with $M_{SC} = 8.088\mu_B$ is found to have the lowest energy, the energy of which is lower than the energies of out-of-plane $M_{SC} = 8.064\mu_B$, out-of-plane $M_{SC} = 0.023\mu_B$, and in-plane $M_{SC} = 0$ configurations by 33, 299, and 384 meV per formula unit, respectively. The latter means that the magnetic anisotropy energy (MAE) is 33 meV per formula unit, which is slightly larger than the predicted value in Ref. [35]. The alignment of the Fe and Te moments in the lowest-energy configuration is *antiparallel* when SOC is taken into account, which is the same as when SOC is ignored.

Now we examine the electronic structure of $FeTe_2$, VS_2, and $NiTe_2$ monolayers in their lowest-energy structures. Figure 5 displays majority and minority spin bands of these three monolayers projected to $d_{x^2-y^2} + d_{xy}$, $d_{xz} + d_{yz}$, and d_{z^2} orbitals of transition-metal atoms and $p_x + p_y$ and p_z orbitals of chalcogen atoms.

The majority spin bands of the $FeTe_2$ monolayer display a metallic behavior with spin-up bands crossing the Fermi level, which are derived mostly from the Te $p_x + p_y$ orbitals with

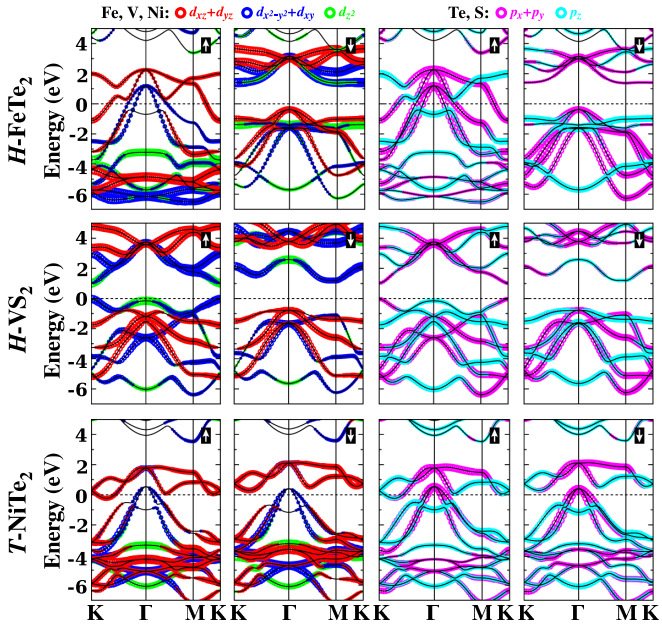

FIG. 5. Orbital projected bands and state densities of majority (↑) and minority (↓) spin states, calculated using HSE, for H-$FeTe_2$ (upper panels), H-VS_2 (middle panels), and T-$NiTe_2$ (lower panels) monolayers. The open circles used to draw spin bands are resized to be proportional to relative contributions from the orbitals of transition-metal (Fe, Ni, and V) and chalcogen (Te and S) atoms, which are also colored as indicated at the top. The zero of energy is set to the Fermi level for metals and to the energy of the highest occupied spin state for semiconductors.

significant contribution from the Fe $d_{x^2-y^2}+d_{xy}$ and $d_{xz}+d_{yz}$ orbitals. The minority spin bands, on the other hand, have an indirect band gap of 1.77 eV. While the top of the valence band at the center of the Brillouin zone slightly below the Fermi energy is derived from the Fe $d_{xz}+d_{yz}$ orbitals, the bottom of the conduction band at the K-point is constructed mostly from the Fe $d_{x^2-y^2}+d_{xy}$ and d_{z^2} orbitals. The Te p_x+p_y orbitals make also a substantial contribution to both the upper valence and lower conduction bands. It seems that the hybridization of the Fe d and Te p orbitals make both the spin-up states around the Fermi level and the spin-down states in the upper valence and lower conduction bands have a significant contribution from the p (d) orbitals of Te (Fe) atoms. This summarized arrangement of spin bands in Fig. 5 shows, in agreement with previous predictions [35], that the $FeTe_2$ monolayer with $\mu_{\rm tot}=2\mu_{\rm B}$ is a *half metal*. Hence the $FeTe_2$ monolayer keeps the promise of being a potential spintronic material operating as a spin valve or an active component in 2D MTJs.

The spin-polarized electronic states of the VS_2 monolayer, on the other hand, display a rather different situation, as also noted by others [72,73,89]: Both spin-up and spin-down bands open a band gap of different widths. The direct band gap of spin-up bands is 1.06 eV and occurs at the K-point. V d_{z^2} and S p_x+p_y orbitals contribute to the spin-up states at the conduction- and valence-band edges. The indirect band gap of spin-down states is 1.98 eV and occurs between the conduction-band states at the M-point derived from V $d_{x^2-y^2}+d_{xy}$ and S p_z orbitals, and the valence-band states at the Γ-point are derived from V $d_{xz}+d_{yz}$ and S p_x+p_y and p_z orbitals. The VS_2 monolayer is thus an interesting 2D structure with an integer magnetic moment of $\mu_{\rm tot}=1\mu_{\rm B}$ and has two band gaps of different width for different spin polarization; one of them is direct, while the other one is indirect. This is a rare situation and offers critical spintronic applications.

Finally, the $NiTe_2$ monolayer in Fig. 5 is metallic for both spin bands, but has spin polarization at the Fermi level and hence a net magnetic moment of $0.11\mu_{\rm B}$. In earlier studies [5,29,30] using only LDA, the $NiTe_2$ monolayer was predicted to be a nonmagnetic metal with a perfect symmetry between spin-up and spin-down densities. Apparently, LDA alone failed to determine the ground state of $NiTe_2$.

In Fig. S2 in the Supplemental Material [88], the electronic structure of $FeTe_2$, VS_2, and $NiTe_2$ monolayers in higher-energy structures is given for completeness. A comparison between this figure and Fig. 5 shows that $NiTe_2$ and VS_2 monolayers are metallic and semiconducting, respectively, *regardless* of the phase (H or T). On the other hand, the $FeTe_2$ monolayer in the T structure is metallic, which shows that the half metallicity of $FeTe_2$ occurs only in the H structure.

Having set the type of the magnetic ground state and predicted half-metallic state of the H-$FeTe_2$ monolayer, we now examine two critical issues, which are of fundamental as well as technological importance since they may offer efficient tunability in electronic properties: How do the magnetic ground state and electronic structure vary with (i) strain and (ii) the number of layers in van der Waals $FeTe_2$ multilayers? In Figs. 6(a)–6(c), S3, and S4 [88], we present the variation of minority band gap $E_g^{\downarrow}$, magnetic moment per formula unit $\mu_{\rm tot}$, and magnetic moment of Fe (Te) atoms $\mu_{\rm Fe}$ ($\mu_{\rm Te}$) with the applied biaxial strain ϵ. Although the T phase remains the higher-energy phase of the $FeTe_2$ monolayer for a wide range of strain ($-0.10\leqslant\epsilon\leqslant 0.10$) as shown in Fig. S5 [88], the results for the T-$FeTe_2$ monolayer are included in Figs. 6(a)–6(c) for comparison. It is seen that the half-metallic state of the H-$FeTe_2$ monolayer determined in equilibrium (i.e., $\epsilon=0$) subsists as long as $-0.07<\epsilon$, but transforms almost suddenly to metallic once $\epsilon\leqslant -0.07$. On the other hand, the metallic state of the T-$FeTe_2$ monolayer transforms to a half-metallic state once $\epsilon>0.03$. In the range of strain where the half-metallic state prevails, the total magnetic moment per formula unit is fixed at $\mu_{\rm tot}=2\mu_{\rm B}$ since $\mu_{\rm Fe}$ and $\mu_{\rm Te}$ increase in reverse directions, which holds true for both H and T phases. For the H-$FeTe_2$ monolayer, these findings point to the fact that its half-metallic state is robust under strain ranging from compressive to tensile.

Our investigation of the electronic and magnetic states of $FeTe_2$ multilayers of various thicknesses, made of n layers, are summarized in Figs. 6(d)–6(f) and S6 [88]. We performed the HSE calculations for $n=1, 2, 3, 4$, as well as for a 3D layered $FeTe_2$ crystal with optimized structure with vertical stacking geometry corresponding to the energy minimum. The crucial outcome of this investigation is, briefly, that the half-metallic state of $FeTe_2$ occurs *only* for $n\leqslant 2$ (i.e., for monolayer and bilayer), which is destroyed as the multilayer gets thicker

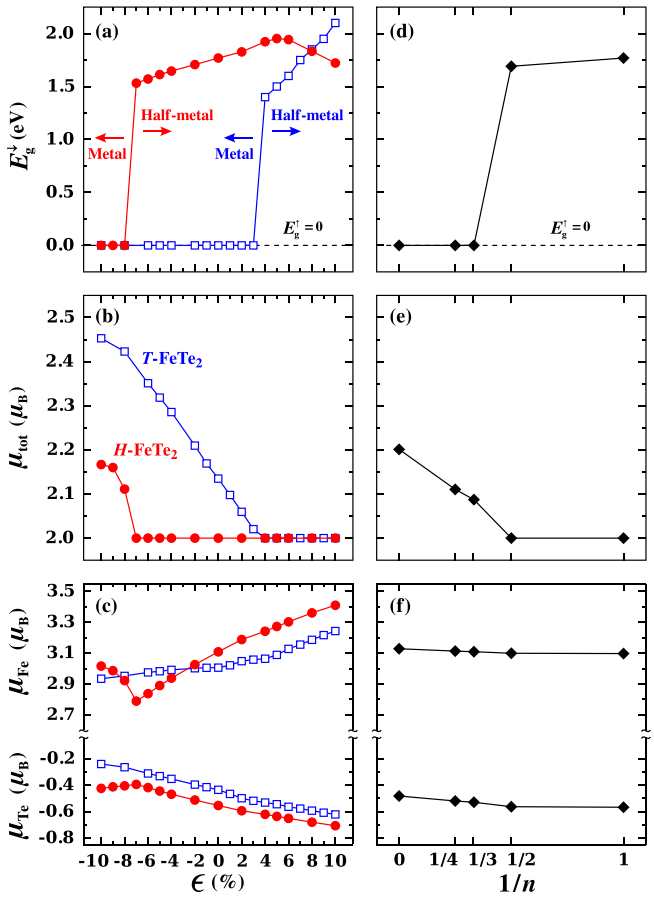

FIG. 6. The variation of (a) the spin-down band gap $E_g^{\downarrow}$, (b) the magnetic moment per formula unit μ_{tot}, and (c) the magnetic moments at Fe and Te atoms, μ_{Fe} and μ_{Te}, respectively, with the biaxial strain ϵ for H-FeTe$_2$ (in red) and T-FeTe$_2$ (in blue) monolayers. (d)–(f) The same with the inverse number of layers $1/n$ for FeTe$_2$ multilayers.

since $E_g^{\downarrow}$ is zero for $n \geqslant 3$. The slight increase in μ_{tot} for $n > 2$ making the total magnetic moment have a noninteger value signifies a transition from the half-metallic state to a magnetic metal, which renders the FeTe$_2$ multilayers thicker than bilayer as magnetic metals.

IV. CONCLUSION

In summary, the true magnetic ground state of three transition-metal dichalcogenide monolayers, viz., FeTe$_2$, VS$_2$, and NiTe$_2$, have been revealed after an extensive first-principles analysis. Our investigation demonstrates that semilocal DFT calculations fail in predicting the ground state of magnetic MX_2 monolayers; the results of DFT + U and hybrid DFT calculations agree on the correct magnetic ground state and magnetic properties of FeTe$_2$ and VS$_2$ monolayers. Remarkably, *both* H and T phases of the foregoing MX_2 monolayers have magnetic ground states with antiparallel alignment of local magnetic moments at M and X atoms owing to the spin polarization of the chalcogen atoms via p-d hybridization. It is clarified that the exchange coupling between the M and X atoms is negative, which may facilitate the use of MX_2 monolayers in spin transfer applications.

Our results indicate that the FeTe$_2$ monolayer in its lowest-energy structure is a half metal, the half metallicity of which can prevail under both compressive and tensile strains. Half metallicity occurs also in FeTe$_2$ bilayers. These properties make FeTe$_2$ monolayers and bilayers promising nanomaterials for spintronic devices such as two-dimensional magnetic tunnel junctions. The VS$_2$ monolayer is a magnetic semiconductor with two different band gaps of different character and widths for spin-up and spin-down states, which can offer critical functionalities in spintronic applications. The NiTe$_2$ monolayer, which used to be known as a nonmagnetic metal, is a magnetic metal with a small magnetic moment. Since chalcogen atoms display similar characters in compounds, we expect other Fe, V, and Ni dichalcogenide monolayers have a similar magnetic ground state. Further studies on ultrathin lateral and vertical composite structures or heterostructures constructed from these magnetic monolayers with intriguing electronic properties and proximity effects can offer interesting research directions.

ACKNOWLEDGMENTS

The calculations reported were performed at the High Performance and Grid Computing Center (TRUBA Resources) of TUBITAK ULAKBIM. S.C. acknowledges financial support from the Academy of Sciences of Turkey (TUBA).

[1] P. Joensen, R. Frindt, and S. Morrison, Single-layer MoS$_2$, Mater. Res. Bull. **21**, 457 (1986).

[2] K. S. Novoselov, D. Jiang, F. Schedin, T. J. Booth, V. V. Khotkevich, S. V. Morozov, and A. K. Geim, Two-dimensional atomic crystals, Proc. Natl. Acad. Sci. USA **102**, 10451 (2005).

[3] K. F. Mak, C. Lee, J. Hone, J. Shan, and T. F. Heinz, Atomically Thin MoS$_2$: A New Direct-Gap Semiconductor, Phys. Rev. Lett. **105**, 136805 (2010).

[4] J. N. Coleman, M. Lotya, A. O'Neill, S. D. Bergin, P. J. King, U. Khan, K. Young, A. Gaucher, S. De, R. J. Smith, I. V. Shvets, S. K. Arora, G. Stanton, H.-Y. Kim, K. Lee, G. T. Kim, G. S. Duesberg, T. Hallam, J. J. Boland, J. J. Wang, J. F. Donegan, J. C. Grunlan, G. Moriarty, A. Shmeliov, R. J. Nicholls, J. M. Perkins, E. M. Grieveson, K. Theuwissen, D. W. McComb, P. D. Nellist, and V. Nicolosi, Two-dimensional nanosheets produced by liquid exfoliation of layered materials, Science **331**, 568 (2011).

[5] C. Ataca, H. Şahin, and S. Ciraci, Stable, single-layer MoX$_2$ transition-metal oxides and dichalcogenides in a honeycomb-like structure, J. Phys. Chem. C **116**, 8983 (2012).

[6] A. Splendiani, L. Sun, Y. Zhang, T. Li, J. Kim, C.-Y. Chim, G. Galli, and F. Wang, Emerging photoluminescence in monolayer MoS$_2$, Nano Lett. **10**, 1271 (2010).

[7] C. Ataca and S. Ciraci, Functionalization of single-layer MoS$_2$ honeycomb structures, J. Phys. Chem. C **115**, 13303 (2011).

[8] B. Radisavljevic, A. Radenovic, J. Brivio, V. Giacometti, and A. Kis, Single-layer MoS_2 transistors, Nat. Nanotechnol. **6**, 147 (2011).

[9] S. Cahangirov, C. Ataca, M. Topsakal, H. Sahin, and S. Ciraci, Frictional Figures of Merit for Single Layered Nanostructures, Phys. Rev. Lett. **108**, 126103 (2012).

[10] B. Hinnemann, P. G. Moses, J. Bonde, K. P. Jørgensen, J. H. Nielsen, S. Horch, I. Chorkendorff, and J. K. Nørskov, Biomimetic hydrogen evolution: MoS_2 nanoparticles as catalyst for hydrogen evolution, J. Am. Chem. Soc. **127**, 5308 (2005).

[11] M. Bernardi, M. Palummo, and J. C. Grossman, Extraordinary sunlight absorption and one nanometer thick photovoltaics using two-dimensional monolayer materials, Nano Lett. **13**, 3664 (2013).

[12] Y. Li, K.-A. N. Duerloo, K. Wauson, and E. J. Reed, Structural semiconductor-to-semimetal phase transition in two-dimensional materials induced by electrostatic gating, Nat. Commun. **7**, 10671 (2016).

[13] C. Zhang, S. KC, Y. Nie, C. Liang, W. G. Vandenberghe, R. C. Longo, Y. Zheng, F. Kong, S. Hong, R. M. Wallace, and K. Cho, Charge mediated reversible metal-insulator transition in monolayer $MoTe_2$ and $W_xMo_{1-x}Te_2$ alloy, ACS Nano **10**, 7370 (2016).

[14] Y. Wang, J. Xiao, H. Zhu, Y. Li, Y. Alsaid, K. Y. Fong, Y. Zhou, S. Wang, W. Shi, Y. Wang, A. Zettl, E. J. Reed, and X. Zhang, Structural phase transition in monolayer $MoTe_2$ driven by electrostatic doping, Nature (London) **550**, 487 (2017).

[15] M. Gibertini, M. Koperski, A. Morpurgo, and K. Novoselov, Magnetic 2D materials and heterostructures, Nat. Nanotechnol. **14**, 408 (2019).

[16] B. Shabbir, M. Nadeem, Z. Dai, M. S. Fuhrer, Q.-K. Xue, X. Wang, and Q. Bao, Long range intrinsic ferromagnetism in two dimensional materials and dissipationless future technologies, Appl. Phys. Rev. **5**, 041105 (2018).

[17] P. W. Anderson, Antiferromagnetism. Theory of superexchange interaction, Phys. Rev. **79**, 350 (1950).

[18] J. B. Goodenough, Theory of the role of covalence in the perovskite-type manganites [La, M(II)]MnO_3, Phys. Rev. **100**, 564 (1955).

[19] D. Xiao, G.-B. Liu, W. Feng, X. Xu, and W. Yao, Coupled Spin and Valley Physics in Monolayers of MoS_2 and Other Group-VI Dichalcogenides, Phys. Rev. Lett. **108**, 196802 (2012).

[20] X. Xu, W. Yao, D. Xiao, and T. F. Heinz, Spin and pseudospins in layered transition metal dichalcogenides, Nat. Phys. **10**, 343 (2014).

[21] C. Gong, L. Li, Z. Li, H. Ji, A. Stern, Y. Xia, T. Cao, W. Bao, C. Wang, Y. Wang *et al.*, Discovery of intrinsic ferromagnetism in two-dimensional van der Waals crystals, Nature (London) **546**, 265 (2017).

[22] B. Huang, G. Clark, E. Navarro-Moratalla, D. R. Klein, R. Cheng, K. L. Seyler, D. Zhong, E. Schmidgall, M. A. McGuire, D. H. Cobden *et al.*, Layer-dependent ferromagnetism in a van der Waals crystal down to the monolayer limit, Nature (London) **546**, 270 (2017).

[23] N. Sivadas, M. W. Daniels, R. H. Swendsen, S. Okamoto, and D. Xiao, Magnetic ground state of semiconducting transition-metal trichalcogenide monolayers, Phys. Rev. B **91**, 235425 (2015).

[24] J. L. Lado and J. Fernández-Rossier, On the origin of magnetic anisotropy in two dimensional CrI_3, 2D Mater. **4**, 035002 (2017).

[25] Z. Liu, L. Ma, G. Shi, W. Zhou, Y. Gong, S. Lei, X. Yang, J. Zhang, J. Yu, K. P. Hackenberg, A. Babakhani, J.-C. Idrobo, R. Vajtai, J. Lou, and P. M. Ajayan, In-plane heterostructures of graphene and hexagonal boron nitride with controlled domain sizes, Nat. Nanotechnol. **8**, 119 (2013).

[26] Y. Gong, J. Lin, X. Wang, G. Shi, S. Lei, Z. Lin, X. Zou, G. Ye, R. Vajtai, B. I. Yakobson, H. Terrones, M. Terrones, B. K. Tay, J. Lou, S. T. Pantelides, Z. Liu, and P. M. Ajayan, Vertical and in-plane heterostructures from WS_2/MoS_2 monolayers, Nat. Mater. **13**, 1135 (2014).

[27] X. Hong, J. Kim, S.-F. Shi, Y. Zhang, C. Jin, Y. Sun, S. Tongay, J. Wu, Y. Zhang, and F. Wang, Ultrafast charge transfer in atomically thin MoS_2/WS_2 heterostructures, Nat. Nanotechnol. **9**, 682 (2014).

[28] K. Chen, X. Wan, J. Wen, W. Xie, Z. Kang, X. Zeng, H. Chen, and J.-B. Xu, Electronic properties of MoS_2-WS_2 heterostructures synthesized with two-step lateral epitaxial strategy, ACS Nano **9**, 9868 (2015).

[29] M. Aras, Ç. Kılıç, and S. Ciraci, Planar heterostructures of single-layer transition metal dichalcogenides: Composite structures, Schottky junctions, tunneling barriers, and half metals, Phys. Rev. B **95**, 075434 (2017).

[30] M. Aras, Ç. Kılıç, and S. Ciraci, Lateral and vertical heterostructures of transition metal dichalcogenides, J. Phys. Chem. C **122**, 1547 (2018).

[31] A. K. Geim and I. V. Grigorieva, van der Waals heterostructures, Nature (London) **499**, 419 (2013).

[32] J. Kang, S. Tongay, J. Zhou, J. Li, and J. Wu, Band offsets and heterostructures of two-dimensional semiconductors, Appl. Phys. Lett. **102**, 012111 (2013).

[33] B. Zhao, W. Dang, Y. Liu, B. Li, J. Li, J. Luo, Z. Zhang, R. Wu, H. Ma, G. Sun, Y. Huang, X. Duan, and X. Duan, Synthetic control of two-dimensional $NiTe_2$ single crystals with highly uniform thickness distributions, J. Am. Chem. Soc. **140**, 14217 (2018).

[34] Q. Liu, F. Fei, B. Chen, X. Bo, B. Wei, S. Zhang, M. Zhang, F. Xie, M. Naveed, X. Wan, F. Song, and B. Wang, Nontopological origin of the planar Hall effect in the type-II Dirac semimetal $NiTe_2$, Phys. Rev. B **99**, 155119 (2019).

[35] X. Sui, T. Hu, J. Wang, B.-L. Gu, W. Duan, and M.-S. Miao, Voltage-controllable colossal magnetocrystalline anisotropy in single-layer transition metal dichalcogenides, Phys. Rev. B **96**, 041410(R) (2017).

[36] J. P. Perdew, K. Burke, and M. Ernzerhof, Generalized Gradient Approximation Made Simple, Phys. Rev. Lett. **77**, 3865 (1996).

[37] S. L. Dudarev, G. A. Botton, S. Y. Savrasov, C. J. Humphreys, and A. P. Sutton, Electron-energy-loss spectra and the structural stability of nickel oxide: An LSDA+U study, Phys. Rev. B **57**, 1505 (1998).

[38] J. Heyd, G. E. Scuseria, and M. Ernzerhof, Hybrid functionals based on a screened Coulomb potential, J. Chem. Phys. **118**, 8207 (2003).

[39] A. V. Krukau, O. A. Vydrov, A. F. Izmaylov, and G. E. Scuseria, Influence of the exchange screening parameter on the performance of screened hybrid functionals, J. Chem. Phys. **125**, 224106 (2006).

[40] M. Aras and Ç. Kılıç, Combined hybrid functional and DFT+U calculations for metal chalcogenides, J. Chem. Phys. **141**, 044106 (2014).

[41] Q. Mao, Y. Zhang, Q. Chen, R. Li, X. Geng, J. Yang, H. Hao, and M. Fang, Metallicity and paramagnetism of single-crystalline NiTe and $NiTe_2$, Phys. Status Solidi B **257**, 1900224 (2020).

[42] Y.-X. Lei, J.-P. Zhou, J.-Z. Wang, N.-X. Miao, Z.-Q. Guo, and Q.-U. Hassan, Novel magnetic properties of uniform $NiTe_x$ nanorods selectively synthesized by hydrothermal method, Mater. Des. **117**, 390 (2017).

[43] I. V. Solovyev, I. V. Kashin, and V. V. Mazurenko, Mechanisms and origins of half-metallic ferromagnetism in CO_2, Phys. Rev. B **92**, 144407 (2015).

[44] R. Logemann, A. N. Rudenko, M. I. Katsnelson, and A. Kirilyuk, Exchange interactions in transition metal oxides: The role of oxygen spin polarization, J. Phys.: Condens. Matter **29**, 335801 (2017).

[45] R. Logemann, A. N. Rudenko, M. I. Katsnelson, and A. Kirilyuk, Non-Heisenberg covalent magnetism in iron oxide clusters, Phys. Rev. Mater. **2**, 073001 (2018).

[46] H. Y. Lv, W. J. Lu, D. F. Shao, Y. Liu, and Y. P. Sun, Strain-controlled switch between ferromagnetism and antiferromagnetism in 1T-CrX_2 (X = Se, Te) monolayers, Phys. Rev. B **92**, 214419 (2015).

[47] R. A. de Groot, F. M. Mueller, P. G. van Engen, and K. H. J. Buschow, New Class of Materials: Half-Metallic Ferromagnets, Phys. Rev. Lett. **50**, 2024 (1983).

[48] S. Wurmehl, H. C. Kandpal, G. H. Fecher, and C. Felser, Valence electron rules for prediction of half-metallic compensated-ferrimagnetic behaviour of Heusler compounds with complete spin polarization, J. Phys.: Condens. Matter **18**, 6171 (2006).

[49] I. Galanakis, P. Mavropoulos, and P. H. Dederichs, Electronic structure and Slater-Pauling behaviour in half-metallic Heusler alloys calculated from first principles, J. Phys. D: Appl. Phys. **39**, 765 (2006).

[50] K. Nakamura, T. Ito, and A. J. Freeman, Half-metallic ferrimagnetism in zincblende Mn-doped transition metal chalcogenides, Phys. Rev. B **72**, 064449 (2005).

[51] R. Weht and W. E. Pickett, Half-metallic ferrimagnetism in Mn_2VAl, Phys. Rev. B **60**, 13006 (1999).

[52] S. Lv, H. Li, D. Han, Z. Wu, X. Liu, and J. Meng, A better ferrimagnetic half-metal $LuCu_3Mn_4O_{12}$: Predicted from first-principles investigation, J. Magn. Magn. Mater. **323**, 416 (2011).

[53] S.-S. Li, S.-J. Hu, W.-X. Ji, P. Li, K. Zhang, C.-W. Zhang, and S.-S. Yan, Emergence of ferrimagnetic half-metallicity in two-dimensional MXene $Mo_3N_2F_2$, Appl. Phys. Lett. **111**, 202405 (2017).

[54] C. Tiusan, T. Dimopoulos, K. Ounadjela, M. Hehn, H. A. M. van den Berg, V. da Costa, and Y. Henry, Correlation between micromagnetism and tunnel magnetoresistance in magnetic tunnel junctions using artificial ferrimagnets, Phys. Rev. B **61**, 580 (2000).

[55] D. W. Abraham, S. S. Parkin, J. C. Slonczewski, and P. L. Trouilloud, Magnetic tunnel junctions using ferrimagnetic materials US Patent No. 6,538,919 (2003).

[56] K. Z. Suzuki, S. Kimura, H. Kubota, and S. Mizukami, Magnetic tunnel junctions with a nearly zero moment manganese nanolayer with perpendicular magnetic anisotropy, ACS Appl. Mater. Interfaces **10**, 43305 (2018).

[57] V. Baltz, A. Manchon, M. Tsoi, T. Moriyama, T. Ono, and Y. Tserkovnyak, Antiferromagnetic spintronics, Rev. Mod. Phys. **90**, 015005 (2018).

[58] B. Balke, G. H. Fecher, J. Winterlik, and C. Felser, Mn_3Ga, a compensated ferrimagnet with high Curie temperature and low magnetic moment for spin torque transfer applications, Appl. Phys. Lett. **90**, 152504 (2007).

[59] C. Graves, A. Reid, T. Wang, B. Wu, S. De Jong, K. Vahaplar, I. Radu, D. Bernstein, M. Messerschmidt, L. Müller *et al.*, Nanoscale spin reversal by non-local angular momentum transfer following ultrafast laser excitation in ferrimagnetic GdFeCo, Nat. Mater. **12**, 293 (2013).

[60] N. Bergeard, V. López-Flores, V. Halte, M. Hehn, C. Stamm, N. Pontius, E. Beaurepaire, and C. Boeglin, Ultrafast angular momentum transfer in multisublattice ferrimagnets, Nat. Commun. **5**, 3466 (2014).

[61] R. Mishra, J. Yu, X. Qiu, M. Motapothula, T. Venkatesan, and H. Yang, Anomalous Current-Induced Spin Torques in Ferrimagnets Near Compensation, Phys. Rev. Lett. **118**, 167201 (2017).

[62] M. Piquemal-Banci, R. Galceran, M.-B. Martin, F. Godel, A. Anane, F. Petroff, B. Dlubak, and P. Seneor, 2D-MTJs: Introducing 2D materials in magnetic tunnel junctions, J. Phys. D: Appl. Phys. **50**, 203002 (2017).

[63] G. Kresse and J. Furthmüller, Efficient iterative schemes for *ab initio* total-energy calculations using a plane-wave basis set, Phys. Rev. B **54**, 11169 (1996).

[64] G. Kresse and D. Joubert, From ultrasoft pseudopotentials to the projector augmented-wave method, Phys. Rev. B **59**, 1758 (1999).

[65] D. M. Ceperley and B. J. Alder, Ground State of the Electron Gas by a Stochastic Method, Phys. Rev. Lett. **45**, 566 (1980).

[66] H. J. Monkhorst and J. D. Pack, Special points for Brillouin-zone integrations, Phys. Rev. B **13**, 5188 (1976).

[67] T. A. Manz and D. S. Sholl, Methods for computing accurate atomic spin moments for collinear and noncollinear magnetism in periodic and nonperiodic materials, J. Chem. Theory Comput. **7**, 4146 (2011).

[68] N. G. Limas and T. A. Manz, Introducing DDEC6 atomic population analysis: Part 4. Efficient parallel computation of net atomic charges, atomic spin moments, bond orders, and more, RSC Adv. **8**, 2678 (2018).

[69] M. Kan, B. Wang, Y. H. Lee, and Q. Sun, A density functional theory study of the tunable structure, magnetism and metal-insulator phase transition in VS_2 monolayers induced by in-plane biaxial strain, Nano Res. **8**, 1348 (2015).

[70] E. B. Isaacs and C. A. Marianetti, Electronic correlations in monolayer VS_2, Phys. Rev. B **94**, 035120 (2016).

[71] Y. Ma, Y. Dai, M. Guo, C. Niu, Y. Zhu, and B. Huang, Evidence of the existence of magnetism in pristine VX_2 monolayers (X = S, Se) and their strain-induced tunable magnetic properties, ACS Nano **6**, 1695 (2012).

[72] H. L. Zhuang and R. G. Hennig, Stability and magnetism of strongly correlated single-layer, Phys. Rev. B **93**, 054429 (2016).

[73] H.-R. Fuh, C.-R. Chang, Y.-K. Wang, R. F. L. Evans, R. W. Chantrell, and H.-T. Jeng, Newtype single-layer magnetic

semiconductor in transition-metal dichalcogenides VX_2 (X = S, Se and Te), Sci. Rep. **6**, 32625 (2016).

[74] M. Lan, G. Xiang, Y. Nie, D. Yang, and X. Zhang, The static and dynamic magnetic properties of monolayer iron dioxide and iron dichalcogenides, RSC Adv. **6**, 31758 (2016).

[75] J. Yang, A. Wang, S. Zhang, J. Liu, Z. Zhong, and L. Chen, Coexistence of piezoelectricity and magnetism in two-dimensional vanadium dichalcogenides, Phys. Chem. Chem. Phys. **21**, 132 (2019).

[76] Y.-R. Jang and B. Deok Yu, Hybrid functional study of the structural and electronic properties of Co and Ni, J. Phys. Soc. Jpn. **81**, 114715 (2012).

[77] M. Schlipf, M. Betzinger, C. Friedrich, M. Ležaić, and S. Blügel, HSE hybrid functional within the FLAPW method and its application to GdN, Phys. Rev. B **84**, 125142 (2011).

[78] Y. Yafet and C. Kittel, Antiferromagnetic arrangements in ferrites, Phys. Rev. **87**, 290 (1952).

[79] J. S. Smart, The Néel theory of ferrimagnetism, Am. J. Phys **23**, 356 (1955).

[80] D. Feng and G. Jin, *Introduction to Condensed Matter Physics* (World Scientific, Singapore, 2005).

[81] B. E. Houari, M. Benhamou, M. E. Hafidi, and G. Chouteau, Para-ferrimagnetic transition in strong coupling paramagnetic systems: Landau theory approach, J. Magn. Magn. Mater. **166**, 97 (1997).

[82] O. N. Mryasov, Magnetic interactions and phase transformations in FeM, M = (Pt, Rh) ordered alloys, Phase Transitions **78**, 197 (2005).

[83] D. S. Rodbell, I. S. Jacobs, J. Owen, and E. A. Harris, Biquadratic Exchange and the Behavior of Some Antiferromagnetic Substances, Phys. Rev. Lett. **11**, 10 (1963).

[84] E. Prince, Biquadratic exchange and the temperature dependence of sublattice magnetization in lithium ferrite, J. Appl. Phys. **36**, 161 (1965).

[85] C. M. Srivastava, G. Srinivasan, and N. G. Nanadikar, Exchange constants in spinel ferrites, Phys. Rev. B **19**, 499 (1979).

[86] H. Pan, Electronic and magnetic properties of vanadium dichalcogenides monolayers tuned by hydrogenation, J. Phys. Chem. C **118**, 13248 (2014).

[87] R. Zhao, T. Wang, M. Zhao, C. Xia, Y. An, and X. Dai, Modulation of the electronic properties and spin polarization of 2H VS_2 nanoribbons by tuning ribbon widths and edge decoration, Phys. Chem. Chem. Phys. **21**, 18211 (2019).

[88] See Supplemental Material at http://link.aps.org/supplemental/10.1103/PhysRevB.101.054429 for the predicted values of Curie temperature for VS_2 and $FeTe_2$ monolayers, a comparison of two parametrizations of E_{SC} as a function of the sublattice magnetic moments using $E_{SC} = E_0 + E_2 + E_4$ and $E_{SC} = E_0 + E_2$ with the E_2 and E_4 terms given in Eq. (1), the energy versus strain curves for H and T phases of the $FeTe_2$ monolayer, and the orbital projected majority and minority spin bands for $FeTe_2$, VS_2, and $NiTe_2$ monolayers in higher-energy structures and the $FeTe_2$ monolayer under biaxial compressive and tensile strains, $FeTe_2$ multilayers, and 3D layered $FeTe_2$ crystal.

[89] P.-R. Huang, Q.-Y. Chen, H. K. Pal, M. Kindermann, C. Cao, and Y. He, Correlated electronic structures of group-V transition metal dichalcogenide monolayers from hybrid density-functional calculations, Superlattices Microstruct. **100**, 997 (2016).